AGU ADVANCING EARTH AND SPACE SCIENCES

Geophysical Research Letters

RESEARCH LETTER
10.1029/2025GL118991

Sound Velocities of FeO-Bearing Ringwoodite and Majorite: Implication for Martian Mantle Seismic Profiles

Luo Li[1], Takayuki Ishii[2], Young Jay Ryu[3], Dongzhou Zhang[3], Stella Chariton[3], Vitali B. Prakapenka[3], and Jung-Fu Lin[1]

[1]Department of Earth and Planetary Sciences, Jackson School of Geosciences, The University of Texas at Austin, Austin, TX, USA, [2]Institute for Planetary Materials, Okayama University, Misasa, Japan, [3]GeoSoilEnviroCARS, University of Chicago, Argonne, IL, USA

Key Points:

- Sound velocities of FeO-rich single-crystal ringwoodite and majorite were measured up to 25 GPa and 700 K
- *Vp* and *Vs* variations are more sensitive to ringwoodite/majorite ratio compared to FeO content and thermal perturbations
- Martian deep-mantle with 67 vol.% ringwoodite and 33 vol.% majorite best match recent InSight seismic profiles

Supporting Information:

Supporting Information may be found in the online version of this article.

Correspondence to:

L. Li and J.-F. Lin,
luo.li@jsg.utexas.edu;
afu@jsg.utexas.edu

Citation:

Li, L., Ishii, T., Ryu, Y. J., Zhang, D., Chariton, S., Prakapenka, V. B., & Lin, J.-F. (2026). Sound velocities of FeO-bearing ringwoodite and majorite: Implication for Martian mantle seismic profiles. *Geophysical Research Letters*, *53*, e2025GL118991. https://doi.org/10.1029/2025GL118991

Received 21 AUG 2025
Accepted 9 JAN 2026

Author Contributions:

Conceptualization: Luo Li, Jung-Fu Lin
Formal analysis: Luo Li
Funding acquisition: Jung-Fu Lin
Investigation: Luo Li, Takayuki Ishii, Young Jay Ryu, Dongzhou Zhang, Stella Chariton, Vitali B. Prakapenka, Jung-Fu Lin
Methodology: Luo Li, Takayuki Ishii, Young Jay Ryu, Dongzhou Zhang, Stella Chariton, Vitali B. Prakapenka, Jung-Fu Lin
Supervision: Jung-Fu Lin
Visualization: Luo Li, Jung-Fu Lin
Writing – original draft: Luo Li

Abstract Compressional and shear wave velocities (*Vp*, *Vs*) of candidate Martian deep-mantle minerals, FeO-rich ringwoodite ($(Mg_{0.66}Fe_{0.34})_2SiO_4$) and majorite ($Mg_{0.75}Fe_{0.10}Al_{0.26}Ca_{0.07}Si_{0.84}O_3$), were measured up to 25 GPa and 700 K using Brillouin light scattering coupled with externally-heated diamond anvil cells. Thermoelastic modeling of our results and literature data along a representative areotherm showed that *Vp* and *Vs* of FeO-bearing ringwoodite are approximately 7.5% and 11.0% higher than that of the majorite. Our results reveal that velocity profiles of these Martian deep-mantle minerals are more sensitive to variations in the ringwoodite/majorite (Mg/Si) ratio than to thermal and FeO chemical perturbations. Our best-fit velocity model to a recent seismic model by Samuel et al. (2023, https://doi.org/10.1038/s41586-023-06601-8) indicates the Martian mantle contains approximately 67 vol.% ringwoodite and 33 vol.% majorite, suggesting a ringwoodite-rich aggregate in the Martian lowermost solid mantle. The ringwoodite-majorite mantle likely co-evolved with the FeO and other incompatible elements in the molten silicate layer above the Martian core-mantle boundary.

Plain Language Summary NASA InSight seismic profiles of the Martian mantle have recently become available and can be compared with laboratory velocity measurements to inform us about the mineralogical and compositional model of the red planet. Ringwoodite and majorite are the two most abundant mineral phases of the Martian deep mantle, in which ringwoodite tends to be relatively rich in FeO while majorite incorporates multiple cations, including Mg, Al, Ca, and Fe. In this study, we report single-crystal elasticity of FeO-rich ringwoodite ($(Mg_{0.66}Fe_{0.34})_2SiO_4$) and majorite ($Mg_{0.75}Fe_{0.10}Al_{0.26}Ca_{0.07}Si_{0.84}O_3$) at high pressure and temperature conditions up to 25 GPa and 700 K. These experimental results enable a comprehensive assessment of seismic velocity profiles in the Martian deep mantle. By integrating our new elastic data with existing models of Martian mantle mineralogy and thermal structures, we calculated velocity profiles for different compositional scenarios. The best-fit model, when compared with available InSight seismic observations, suggests the presence of a ringwoodite-rich aggregate in the lowermost Martian mantle. This composition, characterized by relatively reduced thermal conductivity, lower solidus temperature and enhanced capacity in carrying incompatible elements. The FeO-rich ringwoodite layer co-evolved with the molten FeO-rich silicate layer above the core-mantle boundary that was also reported in recent InSight observations.

1. Introduction

Martian seismic profiles from NASA's InSight Mission have recently revealed a series of exciting observations on its interior (e.g., Banerdt et al., 2020; Lognonné et al., 2020). The InSight Mission deployed the first broadband seismometer on the Martian surface, enabling the detection of over a thousand marsquakes traversing its interior (e.g., Clinton et al., 2018; Horleston et al., 2022). Analyses of these seismic graphs have led to a number of seismic models for the compressional wave and/or shear wave velocity (*Vp* and *Vs*) profiles of the crust, mantle, and core (e.g., Irving et al., 2023; Khan et al., 2023). Of particular interest is the discovery of a low-velocity zone (LVZ), likely a molten FeO-rich silicate layer, of ~150 km thickness above the core-mantle boundary (CMB) (e.g., Anstine & Isayev, 2023; Khan et al., 2023; Samuel et al., 2023). This observation was made possible by analyses of additional marsquakes traversing the LVZ-CMB region and has revised earlier seismic models. This discovery is very significant in our quest to understand the Mars because existence of the LVZ can drastically change our view of the thermal and chemical evolution of the planet. For example, the Martian deep mantle overlying the LVZ appears to be mainly solid and likely co-evolved with LVZ through time, and the LVZ may be

Writing – review & editing: Luo Li, Takayuki Ishii, Young Jay Ryu, Dongzhou Zhang, Jung-Fu Lin

formed from fractional crystallization as a residual of early magma ocean (e.g., Zeff & Williams, 2019). The Martian deep mantle also displays discontinuities at approximately 1,100 and 1,300-km depths, likely corresponding to olivine polymorph transitions (Huang et al., 2022; Khan et al., 2021). At depths below 1,300 km (or ∼15 GPa) where ringwoodite and majorite are expected to become abundant, the *Vs* profile appears to be relatively shallow, while the *Vp* slope is approximately 0.1 km/s per 100 km (Khan et al., 2023; Samuel et al., 2023; Stähler et al., 2021). All these reports signal the importance of knowing the sound velocity profiles of candidate constituent materials at relevant Martian deep mantle depths because their comparisons with the InSight seismic profiles can provide critical constraints on the compositional model and temperature profile of the region.

Based on analyses of Martian meteorites (Shergottites-Nakhlites-Chassignites (SNCs)) and analogies to Earth and chondritic meteorites, Dreibus and Wanke (1985) (often called the DW Model in the literature) proposed a bulk silicate compositional model of the Martian mantle which contains ∼18 wt.% FeO, compared to ∼8 wt.% in Earth's mantle, and Mg# of ∼0.75 (Dreibus & Wanke, 1985). Recent compositional models incorporating meteorite, spacecraft, and/or seismic data show that the FeO content (X_{FeO} = FeO/(MgO + FeO)) of the Martian mantle is ∼21% (Yoshizaki & McDonough, 2020) to ∼19% (Khan et al., 2023). Literature studies have constantly indicated a higher FeO content of 19%–28% and a lower Mg/Si ratio of 0.74–1.03 of the Martian mantle (Ohtani & Kamaya, 1992; Sanloup et al., 1999; Taylor, 2013; Wänke et al., 1984). Together with laboratory high P-T petrological experiments (Bertka & Fei, 1997; Zhou, Olson, et al., 2022), the compositional models of Mars would mean that the deep Martian mantle at ∼1,300–1,500 km depth is mainly made of FeO-rich ringwoodite (e.g., $(Mg_{0.72}Fe_{0.28})_2SiO_4$ in previous petrological experiments) and (Mg,Fe,Ca,Al)-bearing majorite (e.g., $Mg_{0.68}Fe_{0.18}Al_{0.13}Ca_{0.08}Si_{0.92}O_3$) (Bertka & Fei, 1997), possibly together with minor stishovite and calcium perovskite $CaSiO_3$ (Davemaoite). We note that taking the LVZ into consideration, the pressure (depth) of the CMB from recent InSight mission data reaches between 22 and 23 GPa (1,700–1,800 km), which is insufficient for the transformation of ringwoodite and majorite into bridgmanite and ferropericlase (Drilleau et al., 2024; Ishii et al., 2019; Samuel et al., 2023; Yoshizaki & McDonough, 2020). As a result, the ringwoodite and majorite mineralogical assemblage can play a fundamental role in the physical properties and thermal evolution of the Martian deep mantle including the LVZ. Compared to bridgmanite, ringwoodite and majorite exhibit lower sound velocities, reduced viscosity, and distinct thermal transport behavior (e.g., Fu et al., 2023; Hsieh et al., 2017; Mao et al., 2012; Marzotto et al., 2020). Ringwoodite is also known to have relatively high capacity to accommodate water in its lattice as compared to other mantle phases (Inoue et al., 2010; Kohlstedt et al., 1996; Ohtani & Ishii, 2024; Panero, 2010), even though Martian interior is considered to be relatively dry in some studies (Halliday et al., 2001; Shibazaki et al., 2009). These can critically influence the evolution of the Martian mantle, including the mantle convection, the existence of the LVZ, and the source for deep-rooted volcanic activities (e.g., Duncan et al., 2018; ELKINS-TANTON et al., 2003; Hsieh et al., 2024; Zeff & Williams, 2019). Moreover, the rheological and thermal characteristics of these minerals modulate the cooling rates of core and heat flux of CMB, thereby playing a pivotal role in the formation and evolution of the Martian dynamo.

Laboratory velocity-density results on FeO-rich ringwoodite and majorite at relevant pressure-temperature-compositional (P-T-X) conditions are thus critical for understanding the seismic profiles as well as the physical and chemical states of the Martian mantle. For ringwoodite, most of the elasticity data focused on the compositions with ∼10% FeO relevant to Earth's transition zone, and water effect on its elasticity has also been extensively explored using various experimental methods (e.g., Higo et al., 2008; Jacobsen & Smyth, 2006; Mao et al., 2012; Zhou, Zhang, et al., 2022). However, ringwoodite in the Martian deep mantle is expected to be significantly drier and relatively more FeO-rich, such as $(Mg_{0.72}Fe_{0.28})_2SiO_4$ (Bertka & Fei, 1997; Dreibus & Wanke, 1985; Halliday et al., 2001; Shibazaki et al., 2009). Although high-pressure ultrasonic data for ringwoodite aggregate with higher FeO content (up to 50%) exist in separate studies, temperature dependence at simultaneous high pressure conditions has only been partially explored, primarily through isothermal bulk moduli derived from high P-T X-ray diffraction (XRD) (e.g., Higo et al., 2006; Wang et al., 2025). Similarly, the elasticity of end-member majorite $MgSiO_3$ has been investigated through high-pressure measurements (e.g., S. V. Sinogeikin and Bass, 2002). However, these studies have predominantly focused on the $MgSiO_3$ endmember or compositions with Mg/Si ratios close to unity (0.95–1.0). In contrast, majorite within Martian deep mantle exhibits a Mg/Si ratio closer to ∼0.75 and contains appreciable amounts of Al, Ca, and Fe substitutions based on previous compositional models and petrological experiments (e.g., Bertka & Fei, 1997; Dreibus & Wanke, 1985). Moreover, the temperature dependence of elastic properties of garnet only has been explored for MgO- and Al_2O_3-bearing compositions (Liu et al., 2015). Recently, ultrasonic experiments have been used to study velocity

profiles of FeO-rich pyrolitic composition up to 16 GPa and 1373 K (Chauvigné et al., 2025). The limited P-T range, large experimental uncertainties, and use of multiphase assemblages have limited their applications to constrain the mineralogical contents, especially for ringwoodite versus majorite, and potential T-X perturbations in Martian deep mantle. The absence of systematic high P-T elasticity data sets for these abundant Martian deep-mantle phases limits our ability to robustly interpret seismic observations and to constrain the composition, thermal structure, and dynamics of Mars' interior.

In this study, we have determined the single-crystal elasticity of FeO-rich ringwoodite ($(Mg_{0.66}Fe_{0.34})_2SiO_4$) and majorite ($Mg_{0.75}Fe_{0.10}Al_{0.26}Ca_{0.07}Si_{0.84}O_3$), that are of relevant compositions to Martian mantle, using Brillouin light scattering (BLS) in externally heated diamond anvil cells (EHDACs) up to 25 GPa and 700 K. The results are modeled using thermodynamics and thermoelastic equations to constrain the P-T-X effects on the elasticity of both ringwoodite and majorite at relevant Martian deep mantle conditions. Combined with literature data, we calculated the velocity profiles of the Martian mantle based on literature compositional models. When compared with InSight seismic models, these results enable us to quantify the net effects of thermal and chemical perturbations on Martian seismic profiles and provide improved constraints for interpreting current and future geophysical observations. Our results reveal that the velocity profiles of Martian deep mantle with 67 vol.% FeO-rich ringwoodite and 33 vol.% majorite match well with the recent InSight seismic model by Samuel et al. (2023).

2. Experiment

Ringwoodite and majorite single crystals were synthesized using a 1000-ton Kawai-type multi-anvil apparatus at the Institute for Planetary Materials, Okayama University, Japan. The target compositions of these crystals were chosen to allow investigation of compositional effects on the velocity and density profiles of the Martian mantle model based on Dreibus and Wanke model (Dreibus & Wanke, 1985). For the ringwoodite synthesis, a starting powdered mixture of Mg_2SiO_4 forsterite, Fe_2SiO_4 fayalite, $Mg(OH)_2$ brucite, and SiO_2 quartz was ground and loaded into an Au capsule. The forsterite and fayalite samples were synthesized from a mixture of $MgO + SiO_2 = 2{:}1$ (mole) at 1,773 K for 24 hr under atmosphere and from a mixture of $Fe_2O_3 + SiO_2 = 1{:}1$ (mole) at 1,373 K for 12 hr under a Fe-FeO buffer condition, respectively (Ishii et al., 2018). The sample assemblage was compressed to 18 GPa and heated to 1,673 K for 3 hr (run# 1k3908). Similarly, a starting powdered mixture of $MgSiO_3$ enstatite, fayalite, quartz, $Al(OH)_3$ gibbsite, and $CaSiO_3$ pseudowollastonite was compressed to 18 GPa and heated to 2,273 K for 2 hr for the majorite synthesis (run# 1k3931). The enstatite and pseudowollastonite were synthesized at 1673 K for 60 hr and 1,573 K for 24 hr, respectively (Ishii et al., 2011, 2012). A number of recovered crystals with subhedral forms without visible defects or inclusions were selected under an optical microscope. Electron microprobe analyses of the crystals showed ringwoodite with $(Mg_{0.66}Fe_{0.34})_2SiO_4$ composition and majorite with $Mg_{0.75}Fe_{0.10}Al_{0.26}Ca_{0.07}Si_{0.84}O_3$ composition on the oxide basis. Infrared spectroscopy analyses further revealed that ringwoodite contains 0.3 wt.% H_2O and majorite has 0.1 wt.% H_2O, respectively (Figure S5 in Supporting Information S1), which are deemed to be small to have noticeable effects on the velocities (Mao et al., 2012). Their crystal structures are determined to be cubic with the space group *Fd3m* for ringwoodite and the space group *Ia3d* for majorite using single-crystal XRD at the Core Facility Center of National Cheng Kung University. Several selected crystals with an approximate diameter of ~100 μm were then orientated to (100) crystallographic orientation and polished to thin platelets for BLS measurements.

High-pressure and room temperature BLS measurements were performed at the Mineral Physics Laboratory, the University of Texas at Austin (UT Austin) up to 25 GPa using short symmetrical DACs with 500 μm diamond culets (Figure 1, Figure S1–S4 in Supporting Information S1). Rhenium (Re) gasket of 250 μm in thickness was pre-indented to ~60 μm in thickness and a 300 μm hole was subsequently drilled in the pre-indented area. Because the BLS measurements require optically transparent or translucent crystals, we have polished a number of pre-oriented ringwoodite and majorite crystals to ~10 and ~25 μm in thickness, respectively, at which they were optically thin for the BLS measurements. Polished crystal platelets were loaded into the sample chamber and neon gas medium was then introduced into the chamber using the gas loading system at UT Austin. Further experimental details for the BLS measurements can be found in Text S1 in Supporting Information S1.

High P-T BLS and XRD measurements were conducted at three different beamlines (13-BMD, BMC and IDD) of the GeoSoilEnviroConsortium, Advanced Radiation Sources, Argonne National Laboratory. The ringwoodite and majorite crystals were separately loaded into EHDACs, each of which was equipped with an external resistive

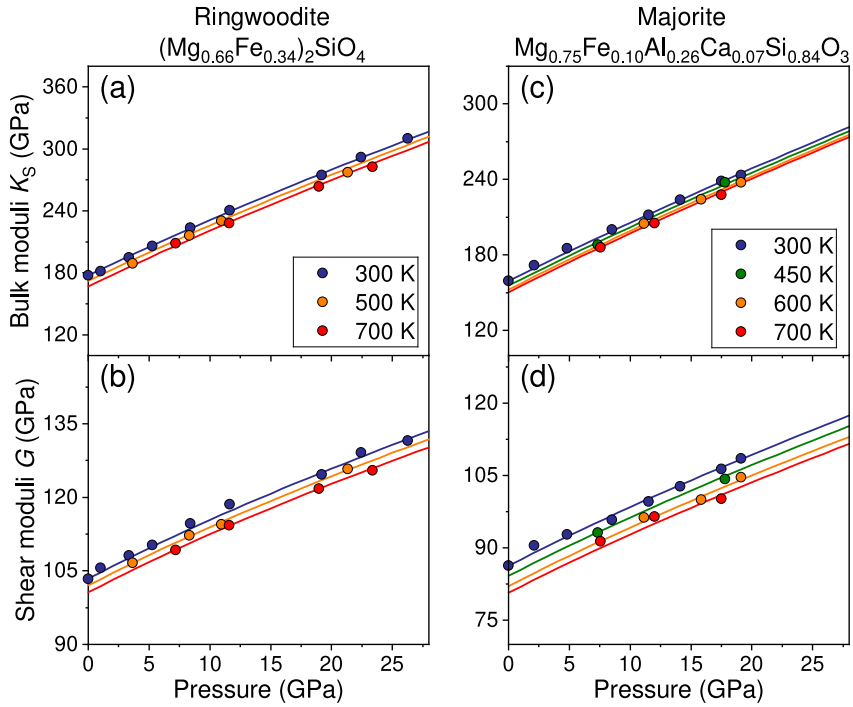

Figure 1. Elastic moduli of Fe-bearing ringwoodite and majorite at high P-T. (a) and (b): K_S and G of ringwoodite [$(Mg_{0.66}Fe_{0.34})_2SiO_4$]; (c) and (d): K_S and G of majorite ($Mg_{0.66}Fe_{0.34}Al_{0.10}Ca_{0.07}Si_{0.84}O_3$); circles and lines: experimental data and finite-strain fitting results.

heater (Pt-Rh wires) and a R-type thermocouple (Kantor et al., 2012; Sinogeikin et al., 2006). A small piece of gold powder of approximately 5 μm big was placed next to the sample and used as the pressure calibrant based on the 3rd-order Birch-Murnaghan thermal equation of state (Fei & Ahrens, 1995). In situ XRD patterns of the crystals were also collected to confirm their orientation of (100) at ∼1 GPa and 300 K before BLS measurements (Table S7 in Supporting Information S1). The EHDAC was placed onto a water-cooled rotatory stage holder to allow alignment of specific crystallographic directions to the direction where the BLS signals are collected. The [100] and [110] crystallographic directions with uncertainties less than 1°, confirmed using in situ XRD patterns, were eventually used for the BLS measurements at 500, 700 K for ringwoodite and 450, 600, 700 K for majorite, respectively. To ensure the pressure stability at each P-T point, we increased the temperature to a given value and waited for at least half an hour before measurements. At each P-T condition, XRD patterns of the crystals were also collected to calculate of their unit cell and thermal equation of state parameters. The collected XRD spectra were integrated into 1-D patterns using DIOPTAS software and the unit cell parameters were calculated using UNITCELL software (Holland & Redfern, 1997; Prescher & Prakapenka, 2015).

3. Results

3.1. Sound Velocities of FeO-Bearing Ringwoodite

Using Christoffel's equation (Text S1 in Supporting Information S1), we have determined the single-crystal elastic constants (C_{ij}s) of ringwoodite up to 25 GPa and 700 K. Combined with the obtained C_{ij}s and synchrotron XRD data, the bulk modulus (K_S), shear modulus (G), V_P and V_S of the ringwoodite were calculated as an isotropic polycrystalline aggregate. All the C_{ij}s, K_S, G, V_P, and V_S were fitted using the third-order finite-strain equation (Text S2 in Supporting Information S1) (Birch, 1978). Ringwoodite within the Martian mantle is relatively more FeO-rich in the solid solution between Mg_2SiO_4 and Fe_2SiO_4, but previous studies only summarized the relationship between elastic parameters and FeO content with the data sets of low FeO content (less than 11.5%). We note that ringwoodite is known to have the high capacity to accommodate water in Earth's transition zone conditions (e.g., Inoue et al., 2010; Kohlstedt et al., 1996; Panero, 2010). The effect of water and FeO on the elasticity of ringwoodite should thus be considered. We firstly modeled the effect of FeO and water on

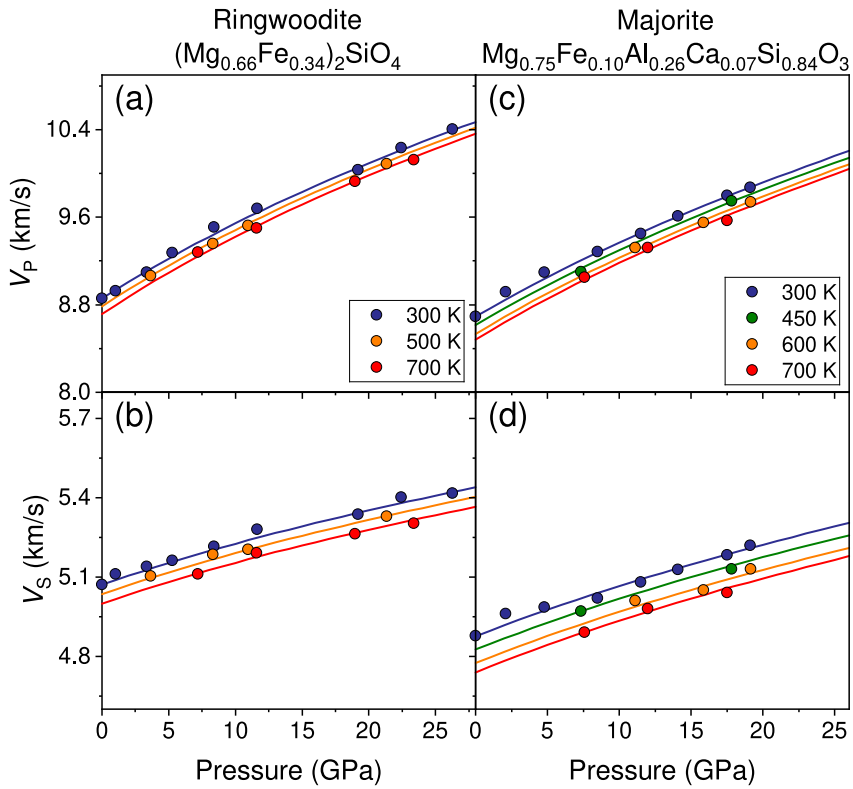

Figure 2. Sound velocity profiles of Fe-bearing ringwoodite and majorite at high P-T. (a) and (b): *Vp* and *Vs* of the ringwoodite phase; (c) and (d): *Vp* and *Vs* of the majorite phase. Circles and solid lines: experimental data and fitting results.

the elasticity of ringwoodite at ambient conditions based on our new experimental data and literature results (Higo et al., 2006, 2008; Huang et al., 2025; Jackson et al., 2000; Schulze et al., 2018; Sinogeikin et al., 2003; Zhou, Zhang, et al., 2022). These analyses show that FeO and water incorporation affect the elastic moduli and density (ρ) following these linear equations (Figure S6 in Supporting Information S1):

$$K_{S0} = 184.0(18) + 10.0(40) \times X_{\mathrm{FeO}} - 9.8(36) \times X_{\mathrm{water}} \quad (1)$$

$$G_0 = 120.0(12) - 38.1(35) \times X_{\mathrm{FeO}} - 6.9(23) \times X_{\mathrm{water}} \quad (2)$$

$$\rho_0 = 3.559(6) + 1.29(21) \times X_{\mathrm{FeO}} - 0.04(1) \times X_{\mathrm{water}} \quad (3)$$

where X_{FeO} is FeO/(MgO + FeO), X_{water} is the water content (wt.%), all the numbers in parentheses were given as one standard deviation. To derive the pressure and temperature derivatives of the elastic moduli (Ks', G', $\partial K_S/\partial T$, and $\partial G/\partial T$) from our data, the elastic parameters of ringwoodite are fitted by the 3rd-order finite strain theory yielding: $K_S' = 5.6(1)$, $G' = 1.3(1)$, $\partial K_S/\partial T = -0.020(1)$ GPa/K and $\partial G/\partial T = -0.010(1)$ GPa/K. We note that K_S' in this study with 34 mol.% FeO is greater than the value of 3.7–4.5(3) for ringwoodite with 0–13.6 mol.% FeO in previous BLS measurements (Jackson et al., 2000; Schulze et al., 2018; Sinogeikin et al., 2003; Zhou, Zhang, et al., 2022). As a result, although the K_{S0} of ringwoodite with 34 mol.% FeO is lower than that of the corresponding FeO-poor ringwoodite, a greater pressure derivative of K_S' leads to a crossover in the K_S at ~5 GPa. Given the well-known trade-off between K_{S0} and K_S' within the finite-strain fitting (e.g., no ambient K_S and K_T data in ultrasonic and XRD experiments, respectively), the effect of FeO on K_{S0} of ringwoodite at ambient conditions is fitted with a fixed K_S' in this study. The values of $\partial K_S/\partial T$ and G' in this study are consistent with previous BLS and ultrasonic results of −0.024 to −0.014 GPa/K and 1.0–1.4, respectively. The strong temperature effect on $\partial K_S/\partial T = -0.038$ GPa/K in Mao et al. (2012) is possible due to high water content of 1.1 wt.%. The G' is within the range of dry ringwoodite results of 1.0–1.4, and greater values of 1.59–1.98 in hydrous ringwoodite are likely involved with different Mg-H/Si-H substitution mechanism (Panero, 2010). Additionally, our

$\partial G/\partial T$ shows a smaller temperature effect than literature results with −0.017 to −0.015 GPa/K, indicating the relatively FeO-rich ringwoodite is denser than its FeO-poor counterpart, while its shear modulus is less sensitive to temperature. Because the elasticity of ringwoodite undergoes a softening at temperatures above 1,200 K, we also used the second-order temperature derivative of the elastic moduli from the literature to calculate the velocity profiles at high P-T conditions (Higo et al., 2008).

3.2. Sound Velocities of Majorite ($Mg_{0.75}Fe_{0.10}Al_{0.26}Ca_{0.07}Si_{0.84}O_3$)

Similar to the ringwoodite elasticity analysis, the elasticity data of the majorite ($Mg_{0.75}Fe_{0.10}Al_{0.26}Ca_{0.07}Si_{0.84}O_3$) up to 25 GPa and 700 K, together with existing literature data, are modeled using the same thermoelastic equations. We also calculated the K_S and G of the majorite aggregate at each P-T condition using the Voigt-Reuss-Hill average. As the second abundant mineral phase within Martian deep mantle, majorite is normally formed as a solid solution between end-member $MgSiO_3$ and $MSiO_3$ (M = Fe, Ca, Al). Our analysis shows that the incorporation of M cations has very complex effects on the elastic parameters (Liu et al., 2000, 2015; Murakami et al., 2008; Pamato et al., 2016; S. V. Sinogeikin and Bass, 2002; Zhou et al., 2021). Here, we focus on the elasticity of majorite along the M cations join while ignoring the influence of Ca with limited data and potential compensation of these elements. As shown in Figure S7 in Supporting Information S1, the substitution of 10 mol.% FeO decreases K_{S0} by 6 GPa but has a minor effect on G_0. The addition of 10 mol.% Al could slightly increase K_{S0} and G_0 by 1 and 1.5 GPa, respectively. These results also indicate no particular effect of water on the elasticity, which is consistent with previous studies (Fan et al., 2019; Liu et al., 2000, 2015; Murakami et al., 2008; Pamato et al., 2016; S. V. Sinogeikin and Bass, 2002; Zhou et al., 2021).

It should be noted that the structures of endmember majorite $MgSiO_3$ and our majorite are tetragonal and cubic, respectively. But the influence of the phase transition on the bulk elastic parameters is within uncertainties at high P-T conditions. The P-T dependence obtained from our experiments are in good agreement with the values reported in the literature with different cation compositions (Table S5 in Supporting Information S1) (Liu et al., 2000, 2015; Murakami et al., 2008; Pamato et al., 2016; S. V. Sinogeikin and Bass, 2002; Zhou et al., 2021). The pressure dependences of K_S' of 4.8(1) and G' of 1.3(1) are within the range from 4.1 to 4.8 in K_S' and 1.1–1.4 in G' compared to previous studies. The high K_S' and G' values reported in Liu et al. (2000) are likely due to non-hydrostatic conditions or the constraints lacking on sample length during the measurements. The derived $\partial K_S/\partial T$ of −0.021(2) GPa/K and $\partial G/\partial T$ of −0.014(1) GPa/K showed greater temperature effects than ultrasonic results in literature (Liu et al., 2015). This may be due to the tradeoff among K_{S0}, K_S' and thermal expansion coefficient in Liu et al. (2015). We have combined the fitted first-order temperature derivative from this study with the second-order temperature derivative of the elastic moduli from the literature data in modeling the velocity profiles at relevant high P-T conditions (Zhou et al., 2021).

4. Discussion and Implications

Our research results were modeled to understand the mineralogical and temperature (compositional and thermal) perturbations of the Martian deep mantle. To start with, we first investigate the effect of thermal perturbations on the velocity profiles of Martian deep mantle minerals using three representative areotherms, namely hot, medium and cold (Figure S9 in Supporting Information S1) (Huang et al., 2022; Plesa et al., 2021). Assuming Martian mantle is adiabatic, the areotherm can be described as (Huang et al., 2022):

$$T(z) = T_0 + T_m \,\mathrm{erf}\left(\frac{z}{\sqrt{kt}}\right) + z\left(\frac{dT}{dz}\right)_{\text{adiabatic}} \tag{4}$$

where T_0 is the surface temperature at 205 K; t is the age at 4.25×10^9 years; κ is the thermal diffusivity of 10^{-6} m^2/s; T_m is the mantle potential temperature (1,200 K (cold), 1,400 K (medium) and 1,600 K (hot)); and $\left(\frac{dT}{dz}\right)_{\text{adiabatic}}$ is the thermal gradient of the mantle adiabatic of 0.12 K/km (see Text S3 in Supporting Information S1 for the selection of parameters). We note that this model is consistent with the areotherms in literature (Plesa et al., 2021). Plesa et al. (2021) explored the impact on the thermal profile of different amounts of heat producing elements in the lithosphere and different thicknesses of the lithosphere. As a result, their areotherms present a stronger thermal gradient in the lithosphere and a hotter mantle than in earlier studies, especially at depth above

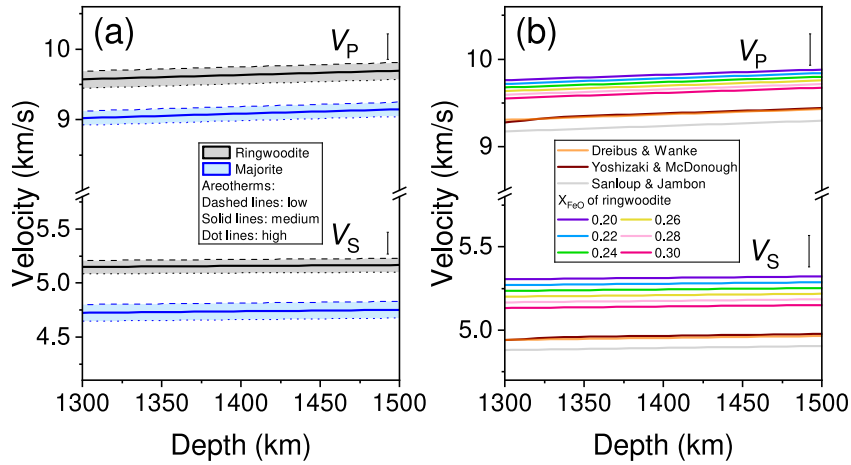

Figure 3. Thermal and FeO chemical perturbations on the velocity profiles of the Martian deep-mantle ringwoodite and majorite. (a) Velocity profiles of ringwoodite and majorite along representative areotherms. The dotted, solid and dashed lines represent the velocity profiles of Martian mantle using high, medium, and low areotherms (see Figure S9 in Supporting Information S1 for details). (b) FeO compositional effects on velocity profiles of ringwoodite. X_{FeO} is the amount of FeO in ringwoodite. The velocity profiles in panel (b) were calculated along medium areotherm. The modeled velocity profiles of the Martian mantle for three compositional models, Dreibus and Wanke (1985) with 25% FeO, Yoshizaki and McDonough (2020) with 21% Fe are also plotted for comparison, Sanloup and Jambon with 25% FeO and Si-enriched (see Figure S10 in Supporting Information S1 for detail). The profiles are calculated using Perple_X program with input data from our high P-T thermoelasticity of ringwoodite and majorite, literature studies, and representative areotherm (Connolly, 2009; Dreibus & Wanke, 1985; Sanloup et al., 1999; Yoshizaki & McDonough, 2020).

500-km. Since the velocity profile of interest here is on the Martian deep mantle, the thermal gradient difference in the shallow depth has been ignored in our model. As shown in Figure 3a, we calculated the *Vp* and *Vs* profiles of the ringwoodite and majorite along cold, medium and hot areotherms which are 200 K differences at 500–1,500 km depths. The *Vp* and *Vs* difference between medium and cold (hot) areotherms is only 0.6% and 0.5%, respectively. Additionally, the temperature effect on the velocities of ringwoodite is smaller than that of majorite. That is, assuming ringwoodite is the most abundant mineral at the deep mantle depths, thermal perturbation of ±200 K, which is within the range of current areotherm models, would only lead to ±0.9% in *Vp* and ±1.0% in *Vs* variation, respectively. These analyses here indicate that if the Martian deep mantle is mainly made of ringwoodite and majorite, a thermal perturbation of ±200 K would have very negligible effects on the *Vp* and *Vs* profiles to be decipherable in current seismic models.

We now considered the compositional effect on velocity profiles. Several compositional models for the Martian mantle have been proposed in previous studies with different FeO content and Mg/Si ratio (Dreibus & Wanke, 1985; Sanloup et al., 1999; Taylor, 2013; Yoshizaki & McDonough, 2020). We firstly examine whether FeO content can apparently affect *Vp* and *Vs* profiles of the ringwoodite. As shown in Figure 3b, increasing X_{FeO} from 0.2 to 0.3 in ringwoodite decreases *Vp* only by ∼2.4% and *Vs* by ∼3.3%, respectively. Taking the experimental and modeling error bars into consideration, the FeO perturbations are well within the uncertainties of seismic resolutions, especially for the bulk Martian mantle. Notably, the results showed that *Vp* and *Vs* of ringwoodite are approximately 6.0% and 8.3% higher than those of the majorite, respectively.

We then conducted further analysis on the effect of Mg/Si ratio on the *Vp* and *Vs* profiles of Martian mantle. Three representative compositional models were considered in this study: the classical model by Dreibus and Wanke (1985) (the DW model), a more recent estimate by Yoshizaki and McDonough (2020) (the YM model) and more silicon-rich model by Sanloup et al. (1999) (the SJ model) (see Figure S10 in Supporting Information S1). Based on the bulk silicate composition of oxides in each model, the corresponding mantle mineralogy was calculated using the thermodynamic modeling software Perple_X version 7.1.12 (Connolly, 2009). The model allows for the determination of mineral proportions in the Martian mantle aggregate as well as element contents through partitioning among relevant mineral phases (Stixrude & Lithgow-Bertelloni, 2022). Thermal modeling was carried out along the same Martian adiabatic areotherm with T_m = 1,400 K. The adiabatic thermal gradient was taken as 0.12 K/km below approximately 500 km depth. These newly obtained elastic parameters

10.1029/2025GL118991

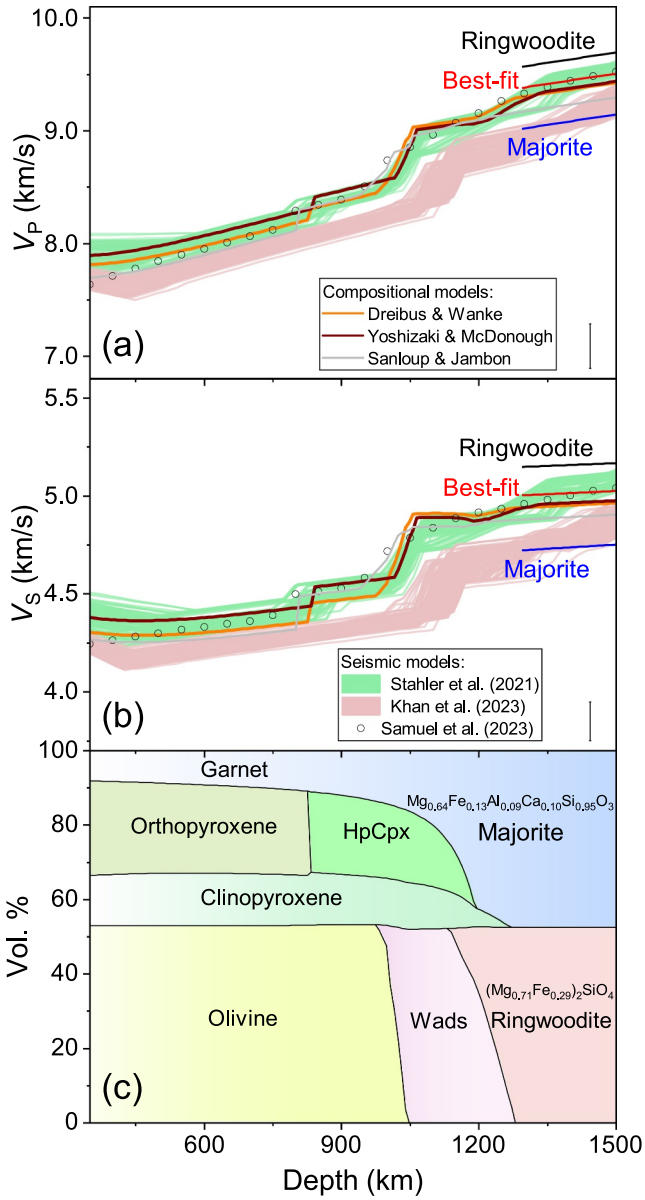

Figure 4. Modeled seismic profiles and mineralogical diagram of the Martian mantle. (a) and (b): the comparison between seismic profiles and calculated velocities of the candidate Martian mantle minerals. The modeled velocity profiles of the constituent mineral phases are calculated using Perple_X program with updated elasticity data from this study. For 1,300–1,500 km depths, the model by Dreibus and Wanke (1985) contains 53 vol.% ringwoodite and 47 vol.% majorite, the model by Yoshizaki and McDonough (2020) contains 48 vol.% ringwoodite and 52 vol.% majorite and the model by Sanloup and Jambon contains 39 vol.% ringwoodite and 61 vol.% majorite (see Figure S10 in Supporting Information S1 for details) (Connolly, 2009; Dreibus & Wanke, 1985; Sanloup et al., 1999; Stixrude & Lithgow-Bertelloni, 2022; Yoshizaki & McDonough, 2020). Best-fit model to Samuel et al.'s seismic profiles (2023) indicates a mineralogical abundance of 67 vol.% ringwoodite and 33 vol.% majorite at 1,300–1,500 km depths. For simplicity in the best-fit model, the compositions of ringwoodite and majorite are fixed using the DW composition. (c) Mineralogical diagram of the Martian mantle. Wads: wadsleyite; HpCpx: high-pressure clinopyroxene. The mineralogical diagram is calculated using Perple_X program with updated elasticity data from this study and DW composition.

were then incorporated into the Perple_X thermodynamic database to generate a self-consistent mineralogical diagram and seismic profiles (see Text S4 and S5 in Supporting Information S1 for details).

As shown in Figure 4, the effect of FeO content (25% in DW model, 21% in YM model and 25% in SJ model) at 300–1,300 km depth is minimal, less than 0.08 km/s for *Vp* and 0.06 km/s for *Vs*, respectively. More notably, the DW model is relatively more olivine-rich and its high-pressure polymorphs compared to YM and SJ model. The calculated *Vp* and *Vs* profiles for the Martian deep mantle at 1,300–1,500 km depths show that the DW model yields slightly lower *Vp* and *Vs* values than the YM model, primarily due to the net effect in mineralogical composition and elastic properties. Compared to the DW and YM models, the SJ model displays relatively lower velocity profiles because of higher silicon and majorite contents. Above ~1,300 km depth, all three models show good agreement with the Martian seismic profiles, within uncertainties, reported by Stähler et al. (2021) and Samuel et al. (2023). However, these velocity profiles are higher than those reported by Khan et al. (2023) through the whole Martian mantle. We note that the velocity profiles of the Martian mantle by Khan et al. (2023) are systematically ~3% lower than those by Stähler et al. (2021) and Samuel et al. (2023). This major discrepancy can be explained by the particular hot mantle temperature profile used in the seismic inversion by Khan et al. (2023). The overestimate on the thermal profile on Martian mantle leads to the lower-than-expected velocity profiles. Interestingly, the velocity profiles in both DW and YM models have very flat *Vs* slopes than seismic *Vs* profiles for Martian deep mantle at 1,300–1,500 km depth. If stishovite and davemaoite with relatively high velocities exist in these regions (Bertka & Fei, 1997) and are taken into consideration, the velocity profiles can be elevated. Further studies on the existence of these phases on seismic profiles and phase equilibrium are needed to reveal further insights into the issue. Additionally, future seismic studies need to provide higher resolution constraints on how velocity profiles change with depth in order to better explain this discrepancy.

Because the observations in Samuel et al. (2023) used more recent data and also explicitly considered the existence of the LVZ, thermo-chemical evolution and melting temperature in their inversion, we further examined the Mg/Si ratio (ringwoodite/majorite) effect on the velocity profiles and the best-fit model to the seismic profiles of Martian deep mantle at 1,300–1,500 km depth based on the following assumptions: (a) the region is only made of ringwoodite and majorite; (b) the composition of the individual phases, ringwoodite ($(Mg_{0.71},Fe_{0.29})_2SiO_4$) and majorite ($Mg_{0.64}Fe_{0.13}Al_{0.09}Ca_{0.10}Si_{0.95}O_3$) are obtained from the DW model at 1500-km depth. Both assumptions are consistent with existing experimental data and thermodynamic modeling results calculated by Perple_X (Bertka & Fei, 1997; Stixrude & Lithgow-Bertelloni, 2022). Our best-fit model to the seismic observations of Samuel et al. (2023) indicates that this region is made of ~67(±5) vol.% ringwoodite and ~33(±5) vol.% majorite (Figure 4). The best-fit model indicates a ringwoodite-rich Martian deep mantle compared to the DW model with 53 vol.% ringwoodite, the YM model with 48 vol.% ringwoodite, and the SJ model with 39 vol.% ringwoodite. As the ringwoodite content increases, the bulk FeO content of the aggregate also increases from 25% in the DW model to 27% in the best-fit model, and the Mg/Si ratio changes from 1.01 to 1.15.

The ringwoodite-rich mineralogical assemblage for the Martian deep mantle can have major implications to the understanding of thermal and chemical

evolution of the Martian interior. In particular, it is naturally co-evolved with the newly detected LVZ of Mars, which has been interpreted as a FeO-rich partially molten silicate layer above the CMB. As illustrated in Figure S12 in Supporting Information S1, a partially molten region with a mixture of lighter silicates and denser FeO-rich melt is expected to occur in the molten layer, where the areotherm intersects the solidus at the interface between the LVZ and the overlying solid mantle (e.g., Elkins-Tanton, 2012; Labrosse et al., 2007; Maurice et al., 2017; Zeff & Williams, 2019). During the long-term cooling and fractional crystallization, buoyant MgO-rich silicates with higher melting temperature crystallize first and float upward, progressively accumulating to form the overlying solid deep mantle. The resulting crystal-rich mushy molten layer is expected to undergo gravitational compaction, expelling interstitial melt back into the bottom and increasing the FeO content and incompatible-element enrichment of the residual melt, analogous to cumulate formation and compaction in magma chambers of lunar magma ocean (Dygert et al., 2017; Namur & Humphreys, 2018; Sim et al., 2024). In contrast, FeO behaves incompatibly and its incorporation into the melt increases melt density while likely decreasing its viscosity compared to MgO-rich counterparts. As a result, the residual molten layer becomes increasingly FeO-rich, denser than the coexisting solid phases and dynamically stable, ultimately evolving into the present-day LVZ (e.g., Ballmer et al., 2017; Collinet et al., 2021; Duncan et al., 2018; Kono et al., 2025; Zeff & Williams, 2019). High P-T petrological experiments on DW composition indicate that melts above the solidus at deep-mantle conditions can reach FeO content of ∼34 mol.%, ∼1.3 times higher than in coexisting solid phases (e.g., Duncan et al., 2018). The overlying solid deep mantle is correspondingly poorer in FeO than the LVZ, yet remains more FeO-rich than the shallower mantle. Our best-fit model therefore provides a plausible composition for this co-evolved ringwoodite-rich deep mantle. Additionally, the FeO-rich assemblage is consistent with current redox conditions of Martian mantle proposed in previous studies. The FeO substitution in solid minerals and melts is known to significantly reduce the thermal conductivity by ∼1 $Wm^{-1}K^{-1}$ and viscosity by ∼0.5 order of magnitude (e.g., Chevrel et al., 2014; Dingwell & Virgo, 1987; Herd et al., 2002; Marzotto et al., 2020; Righter et al., 2008; Xu et al., 2004). The existence of the FeO-rich LVZ and overlaying ringwoodite-rich deep mantle can thus act as a chemical and thermal boundary layer, reducing the CMB heat flux and energy source powering the Martian dynamo while acting as a mantle reservoir for FeO and other incompatible elements. Future direct measurements and simulations on the physical properties of FeO-rich melt and solid phases under relevant P-T conditions are required to better constrain the interior dynamics of Mars. We note that the LVZ inference is primarily based on InSight observations from a single seismic station, and thus its lateral extent and continuity remain uncertain. More seismic constraints are needed to resolve the lateral distribution of the LVZ and assess the dynamic and physical consequences of potential heterogeneity.

Conflict of Interest

The authors declare no conflicts of interest relevant to this study.

Data Availability Statement

Experimental data for Figures 1 and 2, Figure S1–S4 in Supporting Information S1 are listed in Tables S1 to S5 in Supporting Information S1. Detailed experimental results are also available in the Supporting Information S1. Perple_X program 7.1.12 used for thermodynamic modeling is available from: https://www.perplex.ethz.ch/perplex/ibm_and_mac_archives/. All relevant Brillouin data and input file for Perple_X can be downloaded in open research online L. Li (2025).

Acknowledgments
Jung-Fu Lin acknowledges support from Solar System Working Program of National Aeronautics and Space Administration (NASA) (80NSSC23K1274). Takayuki Ishii acknowledges support from the JSPS KAKENHI Grants (Numbers 23K19067, 24K00735, and 25K22047). We thank the Joint-Use User Program of the Institute for Planetary Materials, Okayama University for the sample synthesis (Project number: I24-018). Experiments at GSECARS is supported by NSF EAR –2223273. Part of this research was performed at the Advanced Photon Source, a U.S. Department of Energy Office of Science user facility operated for the Department of Energy Office of Science by Argonne National Laboratory under Contract No. DE-AC02-06CH11357. We acknowledge Tsu-Lien Hung and Jennifer Kung for their experimental assistance with the single-crystal pre-orientation using XRD system at National Cheng Kung University, Taiwan. We acknowledge Kenneth S Befus at UT Austin for the electron microprobe data analyses. We thank Steeve Gréaux for his insights and discussions, which have improved this study. We appreciate constructive comments by two anonymous reviewers and the editor which improved the quality of the paper.

References

Anstine, D. M., & Isayev, O. (2023). Machine learning interatomic potentials and long-range physics. *The Journal of Physical Chemistry A*, *127*(11), 2417–2431. https://doi.org/10.1021/acs.jpca.2c06778

Ballmer, M. D., Houser, C., Hernlund, J. W., Wentzcovitch, R. M., & Hirose, K. (2017). Persistence of strong silica-enriched domains in the Earth's lower mantle. *Nature Geoscience*, *10*(3), 236–240. https://doi.org/10.1038/ngeo2898

Banerdt, W. B., Smrekar, S. E., Banfield, D., Giardini, D., Golombek, M., Johnson, C. L., et al. (2020). Initial results from the InSight mission on Mars. *Nature Geoscience*, *13*(3), 183–189. https://doi.org/10.1038/s41561-020-0544-y

Bertka, C. M., & Fei, Y. (1997). Mineralogy of the Martian interior up to core-mantle boundary pressures. *Journal of Geophysical Research*, *102*(B3), 5251–5264. https://doi.org/10.1029/96jb03270

Birch, F. (1978). Finite strain isotherm and velocities for single-crystal and polycrystalline NaCl at high pressures and 300 K. *Journal of Geophysical Research*, *83*(B3), 1257–1268. https://doi.org/10.1029/jb083ib03p01257

Chauvigné, P., Manthilake, G., Andrault, D., Chantel, J., Gardés, E., Demouchy, S., et al. (2025). Seismic structure of Martian mantle inferred from in situ sound velocity measurements. *Physics of the Earth and Planetary Interiors*, 107378.

Chevrel, M. O., Baratoux, D., Hess, K.-U., & Dingwell, D. B. (2014). Viscous flow behavior of tholeiitic and alkaline Fe-rich martian basalts. *Geochimica et Cosmochimica Acta*, *124*, 348–365. https://doi.org/10.1016/j.gca.2013.08.026

Clinton, J., Giardini, D., Böse, M., Ceylan, S., van Driel, M., Euchner, F., et al. (2018). The Marsquake service: Securing daily analysis of SEIS data and building the Martian seismicity catalogue for InSight. *Space Science Reviews*, *214*(8), 133. https://doi.org/10.1007/s11214-018-0567-5

Collinet, M., Plesa, A. C., Grove, T. L., Schwinger, S., Ruedas, T., & Breuer, D. (2021). MAGMARS: A melting model for the Martian mantle and FeO-rich peridotite. *Journal of Geophysical Research: Planets*, *126*(12), e2021JE006985. https://doi.org/10.1029/2021je006985

Connolly, J. (2009). The geodynamic equation of state: What and how. *Geochemistry, Geophysics, Geosystems*, *10*(10), Q10014. https://doi.org/10.1029/2009gc002540

Dingwell, D. B., & Virgo, D. (1987). The effect of oxidation state on the viscosity of melts in the system Na_2O-FeO-Fe_2O_3-SiO_2. *Geochimica et Cosmochimica Acta*, *51*(2), 195–205. https://doi.org/10.1016/0016-7037(87)90231-6

Dreibus, G., & Wanke, H. (1985). Mars, a volatile-rich planet. *Meteoritics (ISSN 0026-1114), DFG-supported research*, *20*, 367–381.

Drilleau, M., Samuel, H., Garcia, R. F., Rivoldini, A., Perrin, C., Wieczorek, M., et al. (2024). Constraints on lateral variations of Martian crustal thickness from seismological and gravity field measurements. *Geophysical Research Letters*, *51*(4), e2023GL105701. https://doi.org/10.1029/2023gl105701

Duncan, M. S., Schmerr, N. C., Bertka, C. M., & Fei, Y. (2018). Extending the solidus for a model iron-rich Martian mantle composition to 25 GPa. *Geophysical Research Letters*, *45*(19), 10211–210220. https://doi.org/10.1029/2018gl078182

Dygert, N., Lin, J. F., Marshall, E. W., Kono, Y., & Gardner, J. E. (2017). A low viscosity lunar magma ocean forms a stratified anorthitic flotation crust with mafic poor and rich units. *Geophysical Research Letters*, *44*(22), 11282–211291. https://doi.org/10.1002/2017gl075703

Elkins-Tanton, L. T. (2012). Magma oceans in the inner solar system. *Annual Review of Earth and Planetary Sciences*, *40*(1), 113–139. https://doi.org/10.1146/annurev-earth-042711-105503

Elkins-Tanton, L. T., Parmentier, E., & Hess, P. (2003). Magma ocean fractional crystallization and cumulate overturn in terrestrial planets: Implications for Mars. *Meteoritics & Planetary Sciences*, *38*(12), 1753–1771. https://doi.org/10.1111/j.1945-5100.2003.tb00013.x

Fan, D., Xu, J., Lu, C., Tkachev, S. N., Li, B., Ye, Z., et al. (2019). Elasticity of single-crystal low water content hydrous pyrope at high-pressure and high-temperature conditions. *American Mineralogist*, *104*(7), 1022–1031. https://doi.org/10.2138/am-2019-6897

Fei, Y., & Ahrens, T. (1995). Thermal expansion. *Mineral physics and crystallography: a handbook of physical constants*, *2*, 29–44.

Fei, Y., Ricolleau, A., Frank, M., Mibe, K., Shen, G., & Prakapenka, V. (2007). Toward an internally consistent pressure scale. *Proceedings of the National Academy of Sciences*, *104*(22), 9182–9186. https://doi.org/10.1073/pnas.0609013104

Fu, S., Zhang, Y., Okuchi, T., & Lin, J.-F. (2023). Single-crystal elasticity of (Al, fe)-bearing bridgmanite up to 82 GPa. *American Mineralogist: Journal of Earth and Planetary Materials*, *108*(4), 719–730. https://doi.org/10.2138/am-2022-8435

Halliday, A., Wänke, H., Birck, J.-L., & Clayton, R. (2001). The accretion, composition and early differentiation of Mars. *Space Science Reviews*, *96*(1–4), 197–230. https://doi.org/10.1023/a:1011997206080

Herd, C. D., Borg, L. E., Jones, J. H., & Papike, J. J. (2002). Oxygen fugacity and geochemical variations in the Martian basalts: Implications for Martian basalt petrogenesis and the oxidation state of the upper mantle of Mars. *Geochimica et Cosmochimica Acta*, *66*(11), 2025–2036. https://doi.org/10.1016/s0016-7037(02)00828-1

Higo, Y., Inoue, T., Irifune, T., Funakoshi, K.-i., & Li, B. (2008). Elastic wave velocities of $(Mg_{0.91}Fe_{0.09})_2SiO_4$ ringwoodite under P-T conditions of the mantle transition region. *Physics of the Earth and Planetary Interiors*, *166*(3–4), 167–174. https://doi.org/10.1016/j.pepi.2008.01.003

Higo, Y., Inoue, T., Li, B., Irifune, T., & Liebermann, R. C. (2006). The effect of iron on the elastic properties of ringwoodite at high pressure. *Physics of the Earth and Planetary Interiors*, *159*(3–4), 276–285. https://doi.org/10.1016/j.pepi.2006.08.004

Holland, T., & Redfern, S. (1997). Unit cell refinement from powder diffraction data; the use of regression diagnostics. *Mineralogical Magazine*, *61*(1), 65–77. https://doi.org/10.1180/minmag.1997.061.404.07

Horleston, A. C., Clinton, J. F., Ceylan, S., Giardini, D., Charalambous, C., Irving, J. C., et al. (2022). The far side of Mars: Two distant marsquakes detected by InSight. *The Seismic Record*, *2*(2), 88–99. https://doi.org/10.1785/0320220007

Hsieh, W. P., Deschamps, F., Okuchi, T., & Lin, J. F. (2017). Reduced lattice thermal conductivity of Fe-bearing bridgmanite in Earth's deep mantle. *Journal of Geophysical Research*, *122*(7), 4900–4917. https://doi.org/10.1002/2017jb014339

Hsieh, W.-P., Deschamps, F., Tsao, Y.-C., Yoshino, T., & Lin, J.-F. (2024). A thermally conductive Martian core and implications for its dynamo cessation. *Science Advances*, *10*(12), 1–8. https://doi.org/10.1126/sciadv.adk1087

Huang, Q., Schmerr, N. C., King, S. D., Kim, D., Rivoldini, A., Plesa, A.-C., et al. (2022). Seismic detection of a deep mantle discontinuity within Mars by InSight. *Proceedings of the National Academy of Sciences*, *119*(42), e2204474119. https://doi.org/10.1073/pnas.2204474119

Huang, R., Thomson, A. R., Brodholt, J. P., Crichton, W. A., Rosenthal, A., Druzhbin, D., et al. (2025). Sound velocity measurements of γ-$(Mg_{0.91}Fe_{0.09})$ 2SiO4 show that the ringwoodite to bridgmanite and ferropericlase phase transformation does not produce the seismically observed 660 km discontinuity. *Earth and Planetary Science Letters*, *663*, 119416. https://doi.org/10.1016/j.epsl.2025.119416

Inoue, T., Wada, T., Sasaki, R., & Yurimoto, H. (2010). Water partitioning in the Earth's mantle. *Physics of the Earth and Planetary Interiors*, *183*(1–2), 245–251. https://doi.org/10.1016/j.pepi.2010.08.003

Irving, J. C., Lekić, V., Durán, C., Drilleau, M., Kim, D., Rivoldini, A., et al. (2023). First observations of core-transiting seismic phases on Mars. *Proceedings of the National Academy of Sciences*, *120*(18), e2217090120. https://doi.org/10.1073/pnas.2217090120

Ishii, T., Huang, R., Myhill, R., Fei, H., Koemets, I., Liu, Z., et al. (2019). Sharp 660-km discontinuity controlled by extremely narrow binary post-spinel transition. *Nature Geoscience*, *12*(10), 869–872. https://doi.org/10.1038/s41561-019-0452-1

Ishii, T., Kojitani, H., & Akaogi, M. (2011). Post-spinel transitions in pyrolite and Mg_2SiO_4 and akimotoite–perovskite transition in $MgSiO_3$: Precise comparison by high-pressure high-temperature experiments with multi-sample cell technique. *Earth and Planetary Science Letters*, *309*(3–4), 185–197. https://doi.org/10.1016/j.epsl.2011.06.023

Ishii, T., Kojitani, H., & Akaogi, M. (2012). High-pressure phase transitions and subduction behavior of continental crust at pressure–temperature conditions up to the upper part of the lower mantle. *Earth and Planetary Science Letters*, *357*, 31–41. https://doi.org/10.1016/j.epsl.2012.09.019

Ishii, T., Kojitani, H., & Akaogi, M. (2018). Phase relations and mineral chemistry in pyrolitic mantle at 1600-2200°C under pressures up to the uppermost lower mantle: Phase transitions around the 660-km discontinuity and dynamics of upwelling hot plumes. *Physics of the Earth and Planetary Interiors*, *274*, 127–137. https://doi.org/10.1016/j.pepi.2017.10.005

Jackson, J. M., Sinogeikin, S. V., & Bass, J. D. (2000). Sound velocities and elastic properties of γ-Mg_2SiO_4 to 873 K by Brillouin spectroscopy. *American Mineralogist*, *85*(2), 296–303. https://doi.org/10.2138/am-2000-2-306

Jacobsen, S. D., & Smyth, J. R. (2006). Effect of water on the sound velocities of ringwoodite in the transition zone. *Earth's deep water cycle*, *168*, 131.

Kantor, I., Prakapenka, V., Kantor, A., Dera, P., Kurnosov, A., Sinogeikin, S., et al. (2012). BX90: A new diamond anvil cell design for X-ray diffraction and optical measurements. *Review of Scientific Instruments*, *83*(12), 125102. https://doi.org/10.1063/1.4768541

Khan, A., Ceylan, S., van Driel, M., Giardini, D., Lognonné, P., Samuel, H., et al. (2021). Upper mantle structure of Mars from InSight seismic data. *Science*, *373*(6553), 434–438. https://doi.org/10.1126/science.abf2966

Khan, A., Huang, D., Durán, C., Sossi, P. A., Giardini, D., & Murakami, M. (2023). Evidence for a liquid silicate layer atop the Martian core. *Nature*, *622*(7984), 718–723. https://doi.org/10.1038/s41586-023-06586-4

Kohlstedt, D., Keppler, H., & Rubie, D. (1996). Solubility of water in the α, β and γ phases of $(Mg, Fe)_2SiO_4$. *Contributions to Mineralogy and Petrology*, *123*(4), 345–357. https://doi.org/10.1007/s004100050161

Kono, Y., Koyama, C., Kondo, N. M., Ohara, K., Kuwahara, H., Nakada, R., et al. (2025). Gravitational stability of iron-rich peridotite melt at Mars' core-mantle boundary. *Communications Earth and Environment*, *6*(1), 148. https://doi.org/10.1038/s43247-025-02117-3

Labrosse, S., Hernlund, J., & Coltice, N. (2007). A crystallizing dense magma ocean at the base of the Earth's mantle. *Nature*, *450*(7171), 866–869. https://doi.org/10.1038/nature06355

Li, L. (2025). Sound velocities of Fe-bearing ringwoodite and majorite: Implication for Martian Mantle seismic profiles [Dataset]. *Zenodo*. https://doi.org/10.5281/zenodo.17743649

Liu, J., Chen, G., Gwanmesia, G. D., & Liebermann, R. C. (2000). Elastic wave velocities of pyrope–majorite garnets ($Py_{62}Mj_{38}$ and $Py_{50}Mj_{50}$) to 9 GPa. *Physics of the Earth and Planetary Interiors*, *120*(1–2), 153–163. https://doi.org/10.1016/s0031-9201(00)00152-7

Liu, Z., Irifune, T., Gréaux, S., Arimoto, T., Shinmei, T., & Higo, Y. (2015). Elastic wave velocity of polycrystalline $Mj_{80}Py_{20}$ garnet to 21 GPa and 2,000 K. *Physics and Chemistry of Minerals*, *42*, 213–222.

Lognonné, P., Banerdt, W. B., Pike, W. T., Giardini, D., Christensen, U., Garcia, R. F., et al. (2020). Constraints on the shallow elastic and anelastic structure of Mars from InSight seismic data. *Nature Geoscience*, *13*(3), 213–220.

Mao, Z., Lin, J.-F., Jacobsen, S. D., Duffy, T. S., Chang, Y.-Y., Smyth, J. R., et al. (2012). Sound velocities of hydrous ringwoodite to 16 GPa and 673 K. *Earth and Planetary Science Letters*, *331*, 112–119. https://doi.org/10.1016/j.epsl.2012.03.001

Marzotto, E., Hsieh, W. P., Ishii, T., Chao, K. H., Golabek, G. J., Thielmann, M., & Ohtani, E. (2020). Effect of water on lattice thermal conductivity of ringwoodite and its implications for the thermal evolution of descending slabs. *Geophysical Research Letters*, *47*(13), e2020GL087607. https://doi.org/10.1029/2020gl087607

Maurice, M., Tosi, N., Samuel, H., Plesa, A. C., Hüttig, C., & Breuer, D. (2017). Onset of solid-state mantle convection and mixing during magma ocean solidification. *Journal of Geophysical Research: Planets*, *122*(3), 577–598. https://doi.org/10.1002/2016je005250

Murakami, M., Sinogeikin, S. V., Litasov, K., Ohtani, E., & Bass, J. D. (2008). Single-crystal elasticity of iron-bearing majorite to 26 GPa: Implications for seismic velocity structure of the mantle transition zone. *Earth and Planetary Science Letters*, *274*(3–4), 339–345. https://doi.org/10.1016/j.epsl.2008.07.045

Namur, O., & Humphreys, M. C. (2018). Trace element constraints on the differentiation and crystal mush solidification in the Skaergaard intrusion, Greenland. *Journal of Petrology*, *59*(3), 387–418. https://doi.org/10.1093/petrology/egy032

Ohtani, E., & Ishii, T. (2024). Role of water in dynamics of slabs and surrounding mantle. *Progress in Earth and Planetary Science*, *11*(1), 65. https://doi.org/10.1186/s40645-024-00670-7

Ohtani, E., & Kamaya, N. (1992). The geochemical model of Mars: An estimation from the high pressure experiments. *Geophysical Research Letters*, *19*(22), 2239–2242. https://doi.org/10.1029/92gl02369

Pamato, M. G., Kurnosov, A., Ballaran, T. B., Frost, D. J., Ziberna, L., Giannini, M., et al. (2016). Single crystal elasticity of majoritic garnets: Stagnant slabs and thermal anomalies at the base of the transition zone. *Earth and Planetary Science Letters*, *451*, 114–124.

Panero, W. R. (2010). First principles determination of the structure and elasticity of hydrous ringwoodite. *Journal of Geophysical Research*, *115*(B3), B03203. https://doi.org/10.1029/2008jb006282

Plesa, A. C., Bozdağ, E., Rivoldini, A., Knapmeyer, M., McLennan, S. M., Padovan, S., et al. (2021). Seismic velocity variations in a 3D Martian mantle: Implications for the insight measurements. *Journal of Geophysical Research: Planets*, *126*(6), e2020JE006755. https://doi.org/10.1029/2020je006755

Prescher, C., & Prakapenka, V. B. (2015). DIOPTAS: A program for reduction of two-dimensional X-ray diffraction data and data exploration. *High Pressure Research*, *35*(3), 223–230. https://doi.org/10.1080/08957959.2015.1059835

Righter, K., Yang, H., Costin, G., & Downs, R. (2008). Oxygen fugacity in the Martian mantle controlled by carbon: New constraints from the nakhlite MIL 03346. *Meteoritics & Planetary Sciences*, *43*(10), 1709–1723. https://doi.org/10.1111/j.1945-5100.2008.tb00638.x

Samuel, H., Drilleau, M., Rivoldini, A., Xu, Z., Huang, Q., Garcia, R. F., et al. (2023). Geophysical evidence for an enriched molten silicate layer above Mars's core. *Nature*, *622*(7984), 712–717. https://doi.org/10.1038/s41586-023-06601-8

Sanloup, C., Jambon, A., & Gillet, P. (1999). A simple chondritic model of Mars. *Physics of the Earth and Planetary Interiors*, *112*(1–2), 43–54. https://doi.org/10.1016/s0031-9201(98)00175-7

Schulze, K., Marquardt, H., Kawazoe, T., Ballaran, T. B., McCammon, C., Koch-Müller, M., et al. (2018). Seismically invisible water in Earth's transition zone? *Earth and Planetary Science Letters*, *498*, 9–16. https://doi.org/10.1016/j.epsl.2018.06.021

Shibazaki, Y., Ohtani, E., Terasaki, H., Suzuki, A., & Funakoshi, K.-i. (2009). Hydrogen partitioning between iron and ringwoodite: Implications for water transport into the Martian core. *Earth and Planetary Science Letters*, *287*(3–4), 463–470. https://doi.org/10.1016/j.epsl.2009.08.034

Sim, S. J., Hirschmann, M. M., & Hier-Majumder, S. (2024). Volatile and trace element storage in a crystallizing martian magma ocean. *Journal of Geophysical Research: Planets*, *129*(8), e2024JE008346. https://doi.org/10.1029/2024je008346

Sinogeikin, S., Bass, J., Prakapenka, V., Lakshtanov, D., Shen, G., Sanchez-Valle, C., & Rivers, M. (2006). Brillouin spectrometer interfaced with synchrotron radiation for simultaneous X-ray density and acoustic velocity measurements. *Review of Scientific Instruments*, *77*(10), 103905. https://doi.org/10.1063/1.2360884

Sinogeikin, S. V., & Bass, J. D. (2002). Elasticity of majorite and a majorite-pyrope solid solution to high pressure: Implications for the transition zone. *Geophysical Research Letters*, *29*(2), 4-1–4-4. https://doi.org/10.1029/2001gl013937

Sinogeikin, S. V., Bass, J. D., & Katsura, T. (2003). Single-crystal elasticity of ringwoodite to high pressures and high temperatures: Implications for 520 km seismic discontinuity. *Physics of the Earth and Planetary Interiors*, *136*(1), 41–66. https://doi.org/10.1016/s0031-9201(03)00022-0

Stähler, S. C., Khan, A., Banerdt, W. B., Lognonné, P., Giardini, D., Ceylan, S., et al. (2021). Seismic detection of the martian core. *Science*, *373*(6553), 443–448.

Stixrude, L., & Lithgow-Bertelloni, C. (2022). Thermal expansivity, heat capacity and bulk modulus of the mantle. *Geophysical Journal International*, *228*(2), 1119–1149. https://doi.org/10.1093/gji/ggab394

Taylor, G. J. (2013). The bulk composition of Mars. *Geochemistry*, *73*(4), 401–420. https://doi.org/10.1016/j.chemer.2013.09.006

Wang, F., Bausch, H. J., Gardner, L. L., Zhang, D., Armstrong, K., Bell, A. S., et al. (2025). Thermoelastic properties of iron-rich ringwoodite and the deep mantle aerotherm of Mars. *Geophysical Research Letters*, *52*(3), e2024GL109666. https://doi.org/10.1029/2024gl109666

Wänke, H., Dreibus, G., & Jagoutz, E. (1984). Mantle chemistry and accretion history of the Earth. In *Archaean geochemistry: The origin and evolution of the Archaean Continental crust*, edited, (pp. 1–24). Springer.

Xu, Y., Shankland, T. J., Linhardt, S., Rubie, D. C., Langenhorst, F., & Klasinski, K. (2004). Thermal diffusivity and conductivity of olivine, wadsleyite and ringwoodite to 20 GPa and 1373 K. *Physics of the Earth and Planetary Interiors*, *143*, 321–336. https://doi.org/10.1016/j.pepi.2004.03.005

Yoshizaki, T., & McDonough, W. F. (2020). The composition of Mars. *Geochimica et Cosmochimica Acta*, *273*, 137–162. https://doi.org/10.1016/j.gca.2020.01.011

Zeff, G., & Williams, Q. (2019). Fractional crystallization of Martian magma oceans and formation of a thermochemical boundary layer at the base of the mantle. *Geophysical Research Letters*, *46*(20), 10997–11007. https://doi.org/10.1029/2019gl084810

Zhou, C., Gréaux, S., Liu, Z., Higo, Y., Arimoto, T., & Irifune, T. (2021). Sound velocity of $MgSiO_3$ majorite garnet up to 18 GPa and 2000 K. *Geophysical Research Letters*, *48*(14), e2021GL093499. https://doi.org/10.1029/2021GL093499

Zhou, W.-Y., Olson, P. L., Shearer, C. K., Agee, C. B., Townsend, J. P., Hao, M., et al. (2022). High pressure-temperature phase equilibrium studies on Martian basalts: Implications for the failure of plate tectonics on Mars. *Earth and Planetary Science Letters*, *594*, 117751. https://doi.org/10.1016/j.epsl.2022.117751

Zhou, W.-Y., Zhang, J. S., Huang, Q., Lai, X., Chen, B., Dera, P., & Schmandt, B. (2022). High pressure-temperature single-crystal elasticity of ringwoodite: Implications for detecting the 520 discontinuity and metastable ringwoodite at depths greater than 660 km. *Earth and Planetary Science Letters*, *579*, 117359. https://doi.org/10.1016/j.epsl.2021.117359

References From the Supporting Information

Arimoto, T., Gréaux, S., Irifune, T., Zhou, C., & Higo, Y. (2015). Sound velocities of $Fe_3Al_2Si_3O_{12}$ almandine up to 19 GPa and 1700 K. *Physics of the Earth and Planetary Interiors*, *246*, 1–8.

Bass, J. D., & Weidner, D. J. (1984). Elasticity of single-crystal orthoferrosilite. *Journal of Geophysical Research*, *89*(B6), 4359–4371. https://doi.org/10.1029/jb089ib06p04359

Birch, F. (1938). The effect of pressure upon the elastic parameters of isotropic solids, according to Murnaghan's theory of finite strain. *Journal of Applied Physics*, *9*(4), 279–288. https://doi.org/10.1063/1.1710417

Buchen, J., Marquardt, H., Speziale, S., Kawazoe, T., Ballaran, T. B., & Kurnosov, A. (2018). High-pressure single-crystal elasticity of wadsleyite and the seismic signature of water in the shallow transition zone. *Earth and Planetary Science Letters*, *498*, 77–87. https://doi.org/10.1016/j.epsl.2018.06.027

Chen, G., Miletich, R., Mueller, K., & Spetzler, H. A. (1997). Shear and compressional mode measurements with GHz ultrasonic interferometry and velocity-composition systematics for the pyrope-almandine solid solution series. *Physics of the Earth and Planetary Interiors*, *99*(3–4), 273–287. https://doi.org/10.1016/s0031-9201(96)03205-0

Collins, M. D., & Brown, J. M. (1998). Elasticity of an upper mantle clinopyroxene. *Physics and Chemistry of Minerals*, *26*(1), 7–13. https://doi.org/10.1007/s002690050156

Conrad, P. G., Zha, C.-S., Mao, H.-K., & Hemley, R. J. (1999). The high-pressure, single-crystal elasticity of pyrope, grossular, and andradite. *American Mineralogist*, *84*(3), 374–383. https://doi.org/10.2138/am-1999-0321

Duffy, T. S., & Anderson, D. L. (1989). Seismic velocities in mantle minerals and the mineralogy of the upper mantle. *Journal of Geophysical Research*, *94*(B2), 1895–1912. https://doi.org/10.1029/jb094ib02p01895

Duffy, T. S., Zha, C.-s., Downs, R. T., Mao, H.-k., & Hemley, R. J. (1995). Elasticity of forsterite to 16 GPa and the composition of the upper mantle. *Nature*, *378*(6553), 170–173. https://doi.org/10.1038/378170a0

Freitas, D., Manthilake, G., Schiavi, F., Chantel, J., Bolfan-Casanova, N., Bouhifd, M. A., & Andrault, D. (2017). Experimental evidence supporting a global melt layer at the base of the Earth's upper mantle. *Nature Communications*, *8*(1), 2186. https://doi.org/10.1038/s41467-017-02275-9

Fu, S., Yang, J., Tsujino, N., Okuchi, T., Purevjav, N., & Lin, J.-F. (2019). Single-crystal elasticity of (Al, Fe)-bearing bridgmanite and seismic shear wave radial anisotropy at the topmost lower mantle. *Earth and Planetary Science Letters*, *518*, 116–126. https://doi.org/10.1016/j.epsl.2019.04.023

Greaux, S., Irifune, T., Higo, Y., Tange, Y., Arimoto, T., Liu, Z. D., & Yamada, A. (2019). Sound velocity of $CaSiO_3$ perovskite suggests the presence of basaltic crust in the Earth's lower mantle. *Nature*, *565*(7738), 218–221. https://doi.org/10.1038/s41586-018-0816-5

Gréaux, S., Kono, Y., Wang, Y., Yamada, A., Zhou, C., Jing, Z., et al. (2016). Sound velocities of aluminum-bearing stishovite in the mantle transition zone. *Geophysical Research Letters*, *43*(9), 4239–4246. https://doi.org/10.1002/2016GL068377

Hao, M., Zhang, J. S., Zhou, W. Y., & Wang, Q. (2021). Seismic visibility of eclogite in the Earth's upper mantle: Implications from high pressure-temperature single-crystal elastic properties of omphacite. *Journal of Geophysical Research*, *126*(5), e2021JB021683. https://doi.org/10.1029/2021jb021683

Hao, M., Zhang, J. S., Pierotti, C. E., Ren, Z., & Zhang, D. (2019). High-pressure single-crystal elasticity and thermal equation of state of omphacite and their implications for the seismic properties of eclogite in the Earth's interior. *Journal of Geophysical Research*, *124*(3), 2368–2377. https://doi.org/10.1029/2018jb016964

Hao, M., Zhang, J. S., Pierotti, C. E., Zhou, W.-Y., Zhang, D., & Dera, P. (2020). The seismically fastest chemical heterogeneity in the Earth's deep upper mantle—implications from the single-crystal thermoelastic properties of jadeite. *Earth and Planetary Science Letters*, *543*, 116345. https://doi.org/10.1016/j.epsl.2020.116345

Hugh-Jones, D., & Angel, R. (1997). Effect of Ca^{2+} and Fe^{2+} on the equation of state of $MgSiO_3$ orthopyroxene. *Journal of Geophysical Research*, *102*(B6), 12333–12340. https://doi.org/10.1029/96jb03485

Irifune, T., Higo, Y., Inoue, T., Kono, Y., Ohfuji, H., & Funakoshi, K. (2008). Sound velocities of majorite garnet and the composition of the mantle transition region. *Nature*, *451*(7180), 814–817. https://doi.org/10.1038/nature06551

Isaak, D. G., Gwanmesia, G. D., Falde, D., Davis, M. G., Triplett, R. S., & Wang, L. (2007). The elastic properties of β-Mg_2SiO_4 from 295 to 660 K and implications on the composition of Earth's upper mantle. *Physics of the Earth and Planetary Interiors*, *162*(1–2), 22–31. https://doi.org/10.1016/j.pepi.2007.02.010

Jackson, J. M., Sinogeikin, S. V., & Bass, J. D. (2007). Sound velocities and single-crystal elasticity of orthoenstatite to 1073 K at ambient pressure. *Physics of the Earth and Planetary Interiors*, *161*(1), 1–12. https://doi.org/10.1016/j.pepi.2006.11.002

Jiang, F., Speziale, S., Shieh, S. R., & Duffy, T. S. (2004). Single-crystal elasticity of andradite garnet to 11 GPa. *Journal of Physics: Condensed Matter*, *16*(14), S1041–S1052. https://doi.org/10.1088/0953-8984/16/14/014

Jiang, F., Gwanmesia, G. D., Dyuzheva, T. I., & Duffy, T. S. (2009). Elasticity of stishovite and acoustic mode softening under high pressure by Brillouin scattering. *Physics of the Earth and Planetary Interiors*, *172*(3–4), 235–240. https://doi.org/10.1016/j.pepi.2008.09.017

Kung, J., Li, B., Uchida, T., & Wang, Y. (2005). In-situ elasticity measurement for the unquenchable high-pressure clinopyroxene phase: Implication for the upper mantle. *Geophysical Research Letters*, *32*(1), 1–4. https://doi.org/10.1029/2004gl021661

Li, B., & Neuville, D. R. (2010). Elasticity of diopside to 8 GPa and 1073 K and implications for the upper mantle. *Physics of the Earth and Planetary Interiors*, *183*(3), 398–403. https://doi.org/10.1016/j.pepi.2010.08.009

Li, L., Sun, N., Shi, W., Mao, Z., Yu, Y., Zhang, Y., & Lin, J. F. (2022). Elastic anomalies across the α-β phase transition in orthopyroxene: Implication for the metastable wedge in the cold subduction Slab. *Geophysical Research Letters*, *49*(16), e2022GL099366. https://doi.org/10.1029/2022gl099366

Mao, Z., Jacobsen, S. D., Frost, D. J., McCammon, C. A., Hauri, E. H., & Duffy, T. S. (2011). Effect of hydration on the single-crystal elasticity of Fe-bearing wadsleyite to 12 GPa. *American Mineralogist*, *96*(10), 1606–1612. https://doi.org/10.2138/am.2011.3807

Mao, Z., Fan, D., Lin, J.-F., Yang, J., Tkachev, S. N., Zhuravlev, K., & Prakapenka, V. B. (2015). Elasticity of single-crystal olivine at high pressures and temperatures. *Earth and Planetary Science Letters*, *426*, 204–215. https://doi.org/10.1016/j.epsl.2015.06.045

Mayama, N., Suzuki, I., Saito, T., Ohno, I., Katsura, T., & Yoneda, A. (2005). Temperature dependence of the elastic moduli of ringwoodite. *Physics of the Earth and Planetary Interiors*, *148*(2–4), 353–359. https://doi.org/10.1016/j.pepi.2004.09.007

Murakami, M., Hirose, K., Kawamura, K., Sata, N., & Ohishi, Y. (2004). Post-Perovskite phase transition in $MgSiO_3$. *Science*, *304*(5672), 855–858. https://doi.org/10.1126/science.1095932

O'Neill, B., Bass, J. D., Rossman, G. R., Geiger, C. A., & Langer, K. (1991). Elastic properties of pyrope. *Physics and Chemistry of Minerals*, *17*, 617–621.

Plesa, A. C., Padovan, S., Tosi, N., Breuer, D., Grott, M., Wieczorek, M., et al. (2018). The thermal state and interior structure of Mars. *Geophysical Research Letters*, *45*(22), 12198–112209. https://doi.org/10.1029/2018gl080728

Sang, L., & Bass, J. D. (2014). Single-crystal elasticity of diopside to 14GPa by Brillouin scattering. *Physics of the Earth and Planetary Interiors*, *228*, 75–79. https://doi.org/10.1016/j.pepi.2013.12.011

Sinogeikin, S. V., & Bass, J. D. (2000). Single-crystal elasticity of pyrope and MgO to 20 GPa by Brillouin scattering in the diamond cell. *Physics of the Earth and Planetary Interiors*, *120*(1), 43–62. https://doi.org/10.1016/s0031-9201(00)00143-6

Spanovich, N., Smith, M., Smith, P., Wolff, M., Christensen, P., & Squyres, S. (2006). Surface and near-surface atmospheric temperatures for the Mars Exploration Rover landing sites. *Icarus*, *180*(2), 314–320. https://doi.org/10.1016/j.icarus.2005.09.014

Speziale, S., Duffy, T. S., & Angel, R. J. (2004). Single-crystal elasticity of fayalite to 12 GPa. *Journal of Geophysical Research*, *109*(B12), B12202. https://doi.org/10.1029/2004jb003162

Thomas, S.-M., Jacobsen, S. D., Bina, C. R., Reichart, P., Moser, M., Hauri, E. H., et al. (2015a). Quantification of water in hydrous ringwoodite. *Frontiers in Earth Science*, *2*, 38. https://doi.org/10.3389/feart.2014.00038

Thomas, S.-M., Wilson, K., Koch-Müller, M., Hauri, E. H., McCammon, C., Jacobsen, S. D., et al. (2015b). Quantification of water in majoritic garnet. *American Mineralogist*, *100*(5–6), 1084–1092.

Thomson, A. R., Crichton, W. A., Brodholt, J. P., Wood, I. G., Siersch, N. C., Muir, J. M. R., et al. (2019). Seismic velocities of $CaSiO_3$ perovskite can explain LLSVPs in Earth's lower mantle. *Nature*, *572*(7771), 643–647. https://doi.org/10.1038/s41586-019-1483-x

Wang, J., Bass, J. D., & Kastura, T. (2014). Elastic properties of iron-bearing wadsleyite to 17.7GPa: Implications for mantle mineral models. *Physics of the Earth and Planetary Interiors*, *228*, 92–96. https://doi.org/10.1016/j.pepi.2014.01.015

Wang, Z., & Ji, S. (2001). Elasticity of six polycrystalline silicate garnets at pressure up to 3.0 GPa. *American Mineralogist*, *86*(10), 1209–1218. https://doi.org/10.2138/am-2001-1009

Wei, W., Mao, Z., Sun, N., Sun, D., & Tkachev, S. N. (2021). High pressure-temperature single-crystal elasticity of grossular: Implications for the low-velocity layer in the bottom transition Zone. *Geophysical Research Letters*, *48*(9), e2021GL093540. https://doi.org/10.1029/2021gl093540

Zhang, J. S., & Bass, J. D. (2016). Sound velocities of olivine at high pressures and temperatures and the composition of Earth's upper mantle. *Geophysical Research Letters*, *43*(18), 9611–9618. https://doi.org/10.1002/2016gl069949

Zhang, Y., Fu, S., Wang, B., & Lin, J.-F. (2021). Elasticity of a pseudoproper ferroelastic transition from stishovite to post-stishovite at high pressure. *Physical Review Letters*, *126*(2), 025701. https://doi.org/10.1103/physrevlett.126.025701